Thermal Behavior of *Bombyx mori* Silk: Evolution of Crystalline Parameters, Molecular Structure, and Mechanical Properties

A. Martel, M. Burghammer, R. J. Davies, and C. Riekel*

European Synchrotron Radiation Facility, B.P. 220, F-38043 Grenoble Cedex, France

Received August 22, 2007

The thermal behavior up to degradation of *Bombyx mori* silk has been studied by scanning synchrotron radiation microdiffraction, gel electrophoresis, and mechanical testing. The diffraction patterns from single baves can be separated into scattering from anisotropic crystalline β-sheet domains and random short-range order. In contrast to dragline silk, scattering from oriented, short-range-order fibroin is not observed. The sheath of sericin proteins can be selectively probed by a microbeam and shows also principally random short-range-order domains with a small crystalline β-sheet fraction. Microdiffraction experiments on single baves from 100 to 573 K show an increase in lattice expansion along the [010] chain-stacking direction above 200−250 K, which could be due to an increase in side-chain mobility. Degradation of the crystalline fraction commences at approximately 500 K, and the fibers have become amorphous at about 570 K with an onset of carbonization. Gel electrophoresis shows that the degradation of FibH molecules starts already at about 350 K, while FibL molecules start degrading at about 400 K. The mechanical properties of single baves such as strain-to-failure and tensile strength also start degrading at about 400 K, while the initial modulus increases up to about 475 K. It is proposed that this is due to the development of cross-linking in the short-range-order chain fraction.

Introduction

Bombyx mori silk is a semicrystalline biopolymer with a high content (80−85%) of glycine, alanine, and serine.[1−6] It is characterized by a relatively high tensile strength[5,7] and thermal stability.[8,9] *B. mori* silk is composed mainly of three proteins: the fibroin heavy chain (FibH, 350 kDa), the fibroin light chain (FibL, 26 kDa), and the integrity-maintaining glycoprotein P25 (about 30 kDa).[10−12] FibL and FibH are linked by a disulfide bond.[13] These proteins are secreted into the lumen of the posterior silk gland as a molecular complex $(FibH)_6(FibL)_6$-$(P25)_1$ of about 2.3 MDa.[9,10] The two fibroin brins in a bave are kept together by a sheath of sericin proteins, which is composed of several alternative splicing products of the Ser-1 and Ser-2 genes, ranging from 20 to 310 kDa.[14,15] The FibH sequence contains repetitive $[Gly\text{-}Ala\text{-}Gly\text{-}Ser\text{-}Gly\text{-}Ala]_n$ and $[Gly\text{-}Ala\text{-}Gly\text{-}Xaa\text{-}Gly\text{-}Ala]_n$ motifs (Xaa = Tyr, Val, Ser, Ala, or Thr) folding into β-sheets, which are stacked together in crystalline domains. Chain back-folding is thought to occur at irregular Gly-Tyr∼Gly-Tyr sequences.[16] The crystalline domains are at the origin of the poly(alanylglycine) structure of *B. mori* silk.[4] The FibH [Ala-Gly]-rich motifs are separated by a spacer motif having a mainly random-coil predicted secondary structure.[17,18] Spider silks—although different in amino acid composition and functional varieties—have a common origin with insect silks (e.g., *B. mori*).[19,20] This will allow us to draw some parallels in this work. Thus, a hierarchical organization of crystalline and amorphous domains into nanofibrils has been suggested for *B. mori* and *Nephila* dragline silks based on small-angle X-ray scattering (SAXS)[21−23] and small-angle neutron scattering (SANS).[24] Nanofibrils have also been observed for *B. mori* silk by atomic force microscopy (AFM)[22] and transmission electron microscopy (TEM)[25] and for synthetic dragline silk protein by AFM.[26]

The aim of the current work is to determine the thermal behavior of *B. mori* silk up to degradation and to correlate microstructural parameters with macroscopic mechanical behavior. A thermal degradation study has recently been performed for dragline silk, showing a surprisingly high structural stability of β-sheet domains.[27] X-ray structural studies are, however, limited by the semicrystalline nature of silk fibers to the determination of lattice parameters, low-resolution structural modeling, orientation, or nanofibrillar morphology.[23,24,27−29] Molecular models for the macroscopic mechanical behavior of silks use, on the other hand, concepts such as a network of flexible, hydrogen-bonded chains reinforced by crystalline domains,[30] which are only partially accessible to X-ray diffraction analysis. The article will therefore develop, in addition to a crystallographic analysis, methods of separating the short-range-order scattering due to the random chain fraction from the Bragg reflections, using a concept introduced for dragline silk.[29] This will be complimented by a protein analysis on the thermal stability of silk fibroin. Structural studies will be performed by state-of-the art synchrotron radiation (SR) microdiffraction, which allows maximizing the fibroin contribution (see below). The article will introduce several technical advances such as scanning microdiffraction during in situ heating experiments of single brins and baves, the separation of sericin from fibroin scattering at the edge of a bave, and the recursive separation of crystalline and short-range-order peaks in the diffraction patterns.

Materials and Methods

Samples. Fresh *B. mori* cocoons were provided by Unité Séricicole, INRA, Lyon, France, and were used as received. SR microdiffraction experiments were performed on single baves (composed of two brins

* Author to whom correspondence should be addressed. E-mail: riekel@esrf.fr.

10.1021/bm700935w CCC: $37.00
Published on Web 10/20/2007

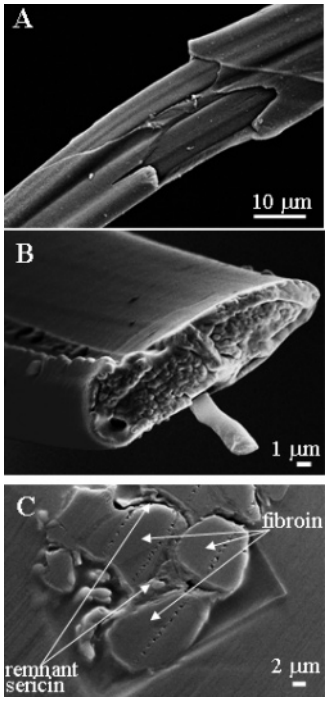

Figure 1. SEM images (ZEISS-LEO 1530; 10 kV HT) of *B. mori* silk samples shadowed by a thin gold-layer: (A) two brins, partially covered by an ~2-μm-thick sericin layer; (B) section of bave cut by a Zeiss/PALM microdissection system. The surface cross-section is 175 μm^2 taking a fiber tilt angle of 45° into account: (C) *Greige* silk containing residual sericin. The sample has been embedded in polymerized (2-hydroxyethyl)-methacrylate resin and cut by an ultramicrotome.

with sericin coating) to maximize fibroin scattering. Such experiments require a high brilliance synchrotron radiation source,[29,31] while experiments with laboratory X-ray sources are limited to fiber bundles.[6,32] The baves were separated from the cocoons with microscissors. Care was taken not to introduce mechanical strain. A SEM image of two brins enveloped partially by a sericin layer is shown in Figure 1A. The cross-section of a bave—produced by laser microdissection—is shown in Figure 1B. The sericin contribution to the bave was determined from the weight loss due to degumming. Approximately 175 mg of baves was degummed in 0.1% Na_2CO_3 at 80 °C for 5 min. The resulting weight loss corresponds to 57 wt % of fibroin, which corresponds also to the fibroin volume fraction assuming equal densities for fibroin and sericin.

Degummed *B. mori* silk was provided by the Stazione Sperimentale per la Seta, Milano.[33] *Greige* silk fibers were provided by Le Musée de la Soie, St. Hippolyte du Fort, France. The sericin layer has been softened and partially removed by boiling the silk fibers in a soap solution (Savon de Marseille) (Figure 1C).

Heating Conditions. Two kinds of heat treatment have been applied, which allow both reversible and irreversible temperature effects to be observed. For in situ synchrotron radiation diffraction experiments under anaerobic conditions, the bave temperature was controlled in the range 100 K < T < 500 K by an Oxford Cryosystems Cryostream 700 system with 5 L/min dry nitrogen flow. The distance of the bave from the nozzle was about 10 mm. The nitrogen gas temperature at the sample position is within 1 K of the cryoflow set temperature for a range of 10 ± 5 mm.[34] Other baves from a cocoon were initially oven-heated before their characterization by electrophoresis, synchrotron radiation diffraction, and mechanical tests. Heating was performed under anaerobic conditions (N_2) up to 473 K and in air for higher temperatures. For protein analysis, mechanical tests, and complimentary diffraction experiments, baves were preheated in an oven for 6 h either under a nitrogen atmosphere (298 K < T < 473 K) or in air (473 K < T < 573 K) and then cooled to room temperature.

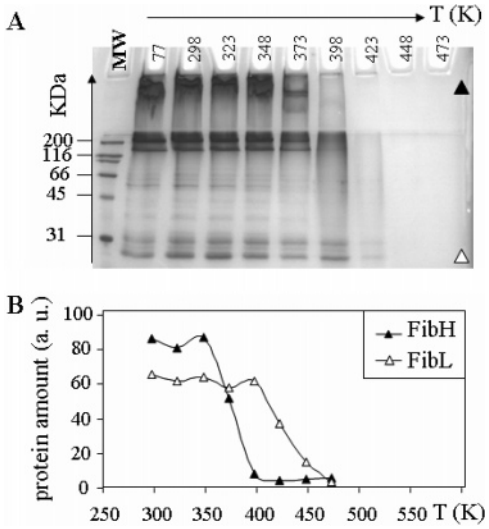

Figure 2. (A) Protein degradation with the temperature from a denaturing 12% polyacrylamide gel electrophoresis (SDS-PAGE); (B) quantification of data shown in part A (MW, molecular weight standard). Black triangles represent FibH, and white triangles FibL.

Gel Electrophoresis. After being heated in a nitrogen atmosphere (as described above), 15 mg of cocoons were partially dissolved in 600 μL of saturated LiSCN under shaking at 60 °C for 3 min. Approximately 3 μL was denatured by boiling 5 min in a 4% β-mercaptoethanol solution and loaded on a 12% denaturing acrylamide gel. The migration lasted 90 min at 120 V. After Coomassie blue staining, an image of the gel was digitized to quantify the relative amount of protein using the FIT2D software.[35] A background line, close to each signal line and having the same size, was subtracted. The results (Figure 2A) are based on the average of three similar experiments. The molecular weight standard is the sodium dodecyl sulfate polyacrylamide gel electrophoresis (SDS-PAGE) standard, broad range, from Biorad. This method reveals the length of the peptides present in the sample, which means, in this case, the integrity of the peptidic chains of FibH and FibL (Figure 2B).

Mechanical Test. Stress−strain curves of single baves were obtained ex situ using a custom-built stretching cell comprising a force sensor and PC-controlled linear translation stage. A 4-mm-long bave was fixed within a cardboard window using cyanoacrylate adhesive. This was then secured to the stretching cell's clamps between the stage and the force sensor. The baves were deformed in tension at a constant rate of extension (10 μm/s) with the force and extension recorded every 0.5 s. The resulting data were then used to calculate fiber stress and strain. For the stress calculations, the cross-sectional area was approximated using a rectangle, which is supported by the SEM micrograph shown in Figure 1B. The rectangle's dimensions were determined microscopically using the AnalySIS5 software package (Soft Imaging System GmbH, Germany), and averaged between three fibers for each temperature. The contribution of the fibroin bins to the total cross-section was assumed to be 57% (see above). The strain-to-failure, stress-to-failure, and Young's modulus were derived from an average of 9−15 stress−strain curves for each temperature. We did not find a significant influence of a shorter gauge length on these mechanical parameters.

Synchrotron Radiation Scattering. Experiments on single *B. mori* baves and brins were performed at the ESRF-ID13 beamline.[36] For the in situ heating experiments a microgoniometer setup was used.[37] The monochromatic synchrotron radiation beam (wavelength, $\lambda = 0.095$ nm; band-pass, $\Delta\lambda/\lambda \approx 2 \times 10^{-4}$-) was focused and collimated to 4 μm for the fresh baves and 10 μm for the *Greige* silk by a combination of compound refractive Be lenses[38] and apertures. A single *B. mori* bave was glued to a thin metal ring, which was attached to a support and aligned in the beam. The temperature of the cryoflow system was ramped in steps of 10 K in the range of 100 K < T < 500 K. At every temperature plateau, a linear scan across the bave with 5 μm steps was

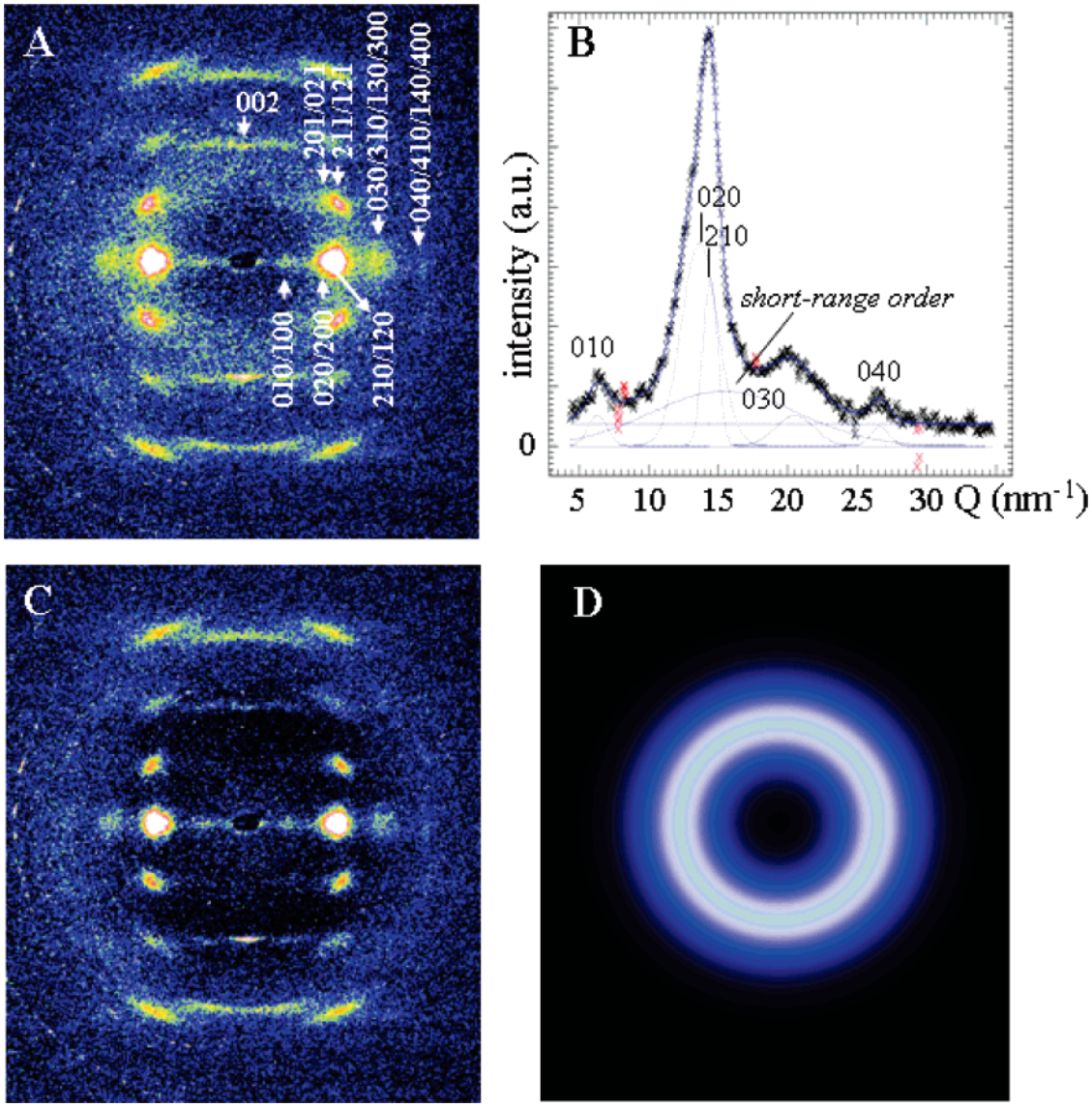

Figure 3. (A) Degummed *B. mori* pattern with Miller's indices for the strongest Bragg peaks. Overlapping reflections are indicated with the most intense equatorial reflections in bold (see text); (B) azimuthally integrated equatorial pattern (crosses) fitted by four narrow Gaussian profiles for the most intense Bragg peaks, a broad Gaussian profile for the short-range-order halo, and a zero-order polynomial (blue lines); (C) degummed *B. mori* pattern after subtraction of the amorphous halo; (D) simulated short-range-order halo (same intensity scale for all patterns). The red data points were masked during refinement.

performed. Consecutive linear scans with increasing temperature were performed displaced by a 13 μm step increment along the bave to avoid possible radiation damage by neighboring scans. The same data collection method was applied to the preheated baves at room temperature. The sample was composed in this case of 12 baves heated at 12 temperatures from 298 to 548 K and glued by both ends on cardboard, which was fixed to the goniometer support. A further bave—heated at 573 K—was too fragile to be fixed in this way and was therefore glued to the end of a tapered capillary. Seven to eight linear scans of 4 μm step increments were performed across each bave, spaced by 20−100 μm along the bave. Complimentary mesh-scanning experiments on fresh or degummed baves and brins were performed at room temperature using a focused beam of approximately 1 μm full width at half-maximum (fwhm) from crossed mirrors or 3 μm fwhm from a tapered glass capillary.[36] Assuming a fiber diameter of 5 μm and a 1 μm in diameter circular beam, this corresponds to about 6×10^9 *B. mori* unit cells[39] in the gauge volume. Micrometer-sized SR beams are too large to resolve banding effects observed in degummed *B. mori* silk by TEM[25] but should be accessible to nanodiffraction SR experiments, which would reduce the number of unit cells probed to the 10^7 level.[40,41] Diffraction patterns were recorded by a slow-scan 16-bit readout MAR165 charge coupled device (CCD) detector. The sample-to-detector distance was calibrated by an Al_2O_3 or Ag−behenate powder[42] standard. Care was taken to avoid radiation damage effects by limiting the data collection time to a few seconds per pattern. Initial data reduction and analysis of individual patterns was performed using the FIT2D software package.[35] For recursive data analysis batch processing software[43] and specialists software (Supporting Information) were used. The instrumental background was corrected by subtracting a pattern recorded just outside a silk fiber during a scan. Sample statistics were improved by averaging several patterns from within the sample and from the background patterns.

Results and Discussion

Microdiffraction from Single Baves and Brins. The fibroin pattern from the center of a degummed *B. mori* brin obtained at room temperature with a 1 μm fwhm beam shows the Bragg peaks of the silk II structure corresponding to the antipolar−antiparallel β-sheet structure[1,4,6] (Figure 3A). We note that this pattern is typical of all other patterns recorded and that in

particular no evidence for a different unit cell or sharper reflections due to larger crystallites, as proposed for dragline silk,[44] was obtained. The pattern can be indexed for a monoclinic $P2_1$ space group with the unit cell:[6] $a = 0.938$ nm, $b = 0.949$ nm, $c = 0.698$ nm (fiber axis); $\gamma \approx 90°$. In the following we will limit the discussion to the 010, 020, 210, and 030 equatorial reflections, which are the only ones observed in diffraction experiments on doubly oriented samples.[6]

One of the aims of the present paper is to determine the evolution of the crystalline and amorphous fibroin fractions with temperature. A quantitative determination of the crystallinity can be performed for two-phase polymers of known composition based on global fit to a one-dimensional (1D) profile.[45] This approach is, however, not adapted to multiple pattern analysis and for the *B. mori* samples where the amino acid composition of amorphous and crystalline fractions is not well-defined. The approach taken in this work is to separate Bragg peaks and short-range-order scattering by a recursive fit of Gaussian functions, which provides information on the profile parameters peak position, peak width, and integrated peak intensity but neglects the contribution of incoherent scattering. The sum of the Bragg peak intensities ($\sum I_{\mathrm{Bragg}}$) will be assumed to be proportional to the crystalline fraction.

For the model of a flexible protein chain matrix, reinforced by crystalline β-sheet domains,[30] one expects a diffuse powder ring due to short-range-order and Bragg peaks. This holds also for short-segment nanofibrils[24] as reinforcing elements. The expected diffuse ring is observed for dragline silk[28,46] and also for the *B. mori* pattern (Figure 3A). The short-range-order peak is related to chain−chain correlation constrained by interchain hydrogen bonding, which may explain that the short-range-order peak position is close to the β-sheet 210 peak position. We note that the short-range-order peak position changes at higher temperatures as the hydrogen-bonding network breaks down (see below). The short-range-order peak can be enhanced in *B. mori* by graft copolymerization of molecules such as methylacrylamide, which are incorporated into the random chain fraction.[33] We have therefore chosen to include the short-range-order peak in the peak profile fitting procedure, in contrast to a recent study on dragline silk.[27]

The quality of this approach will be shown below for a single pattern while details of the specialists' batch processing software are given in the Supporting Information. The equatorial intensity distribution is first azimuthally integrated over an angular range of ∼4°, which covers completely the equatorial reflections and a segment of the diffuse ring. The resulting 1D intensity distribution is fitted by Gaussian profiles for the Bragg peaks and the diffuse peak as well as a zero-order polynomial background for the residual background scattering from the sample (Figure 3B). The use of a homogeneous 210 reflection profile[47] does not result in a stabile profile fit to the asymmetric 200/210 intensity profile including the short-range-order background.

The apparent particle sizes (L) determined by Scherrer's equation[29,48] for the 020 reflection ($L = 1.8$ nm) and the β-sheet 210 reflection ($L = 4.2$ nm) show an increased coherence length along the hydrogen-bonded [210] direction as compared to the β-sheet stacking [010] direction, which is also the case for single dragline silk fibers analyzed according to the same protocol.[29] The L-values for *B. mori* (this work) and for *Nephila* dragline silk[29,46] fit well with molecular modeling predictions for a flexible network reinforced by nanocrystalline domains.[30] It is interesting to compare these particle size values with other values from the literature. X-ray microdiffraction results on *Nephila* dragline silk neglecting the short-range-order scattering suggest values of $L \approx 5$ nm at room temperature for both the [010] and the [210] directions.[27] (Note the exchange of *a* and *b* in ref 27 as compared to the present axis choice for *Nephila*.[29]) TEM dark field (DF) images based on the 020 reflection reveal significantly larger lateral sizes of β-sheet crystallites of about 10 nm.[25] It cannot, however, be excluded that TEM sample preparation (embedding or sectioning) and/or sample exposure to vacuum (dehydration) induces lateral aggregation across the [010] β-sheet stacking direction via van der Waals forces. It has already been noted that L-values determined from dry *Nephila* silk fibers[28] by X-ray diffraction are systematically larger than L-values determined during in situ extrusion.[46] We tentatively assume that the nanocrystalline fibroin domains can assemble axially through a short-range-order interface into nanofibrils but lack the driving force for lateral aggregation, presumably due to a hydration of the nanofibrillar surface. We note in this respect the formation of the *B. mori* silk structure from regenerated sheared fibroin solution through at least one intermediary hydrated phase.[49] Dehydration could therefore result in a further lateral aggregation through van der Waals forces. This scheme is speculative at present but could be tested by systematic aggregation studies.

The axial sizes of β-sheet crystallites in *B. mori* observed by TEM DF images show a large spread from ∼20 to 160 nm.[25] The deduction of rodlike aggregates with axial dimensions of about 170 nm for *Nephila* dragline silk from SANS data[24] suggests that the axial dimensions of *B. mori* crystallites derived by TEM DF[25] are not affected by aggregation.

The diffuse peak ($d \approx 0.41$ nm) is attributed to randomly distributed, short-range-order domains. The 1D Gaussian profile parameters of the short-range-order peak in Figure 3B allow generating a two-dimensional (2D) Gaussian profile (Figure 3D). The subtraction of this profile from the *B. mori* pattern provides a pattern that is a good approximation to a completely crystalline pattern. The intensity of the short-range-order peak (Figure 3D) corresponds to 44% of the total integrated intensity of the raw *B. mori* pattern (Figure 3A), which implies an integrated intensity value of ∼56% for the Bragg peaks. We note that the value of ∼56%—as other values reported in the literature based on more or less extensive peak separation procedures[5,32,50−53]—does not correspond to an exact determination of crystallinity.

It is also interesting to verify the presence of axially oriented, short-range-order domains, which have been proposed connecting the crystalline domains of the nanofibrils in *Nephila* dragline silk.[23,24,28,29] The analysis was performed for the cake-regrouped (transformation of radial and azimuthal scales into orthogonal scales) *B. mori* pattern covering the strongest equatorial and first-layer line reflections (Figure 4A). The pattern can be fitted by four 2D Gaussian profiles for the Bragg peaks and a Gaussian profile for the equatorial diffuse scattering extending from the position of the equatorial peaks to smaller Q-values (Figure 4B). No evidence for additional short-range-order scattering at the position of the 210 reflection is, however, observed in contrast to the 210 reflection of a *Nephila* silk fiber[29] (see remark on unit cell choice above). We attribute this to a lower volume fraction of short-range-order domains in *B. mori* as compared to dragline silk,[46] presumably due to its higher crystallinity.[28] This implies in the frame of the nanofibrillar model[24] longer crystalline domains and shorter short-range-order interface domains, which agrees with SAXS analysis of *B. mori* silk[54] and SAXS/WAXS data of dragline silk (see discussion particle size values above and ref 46).

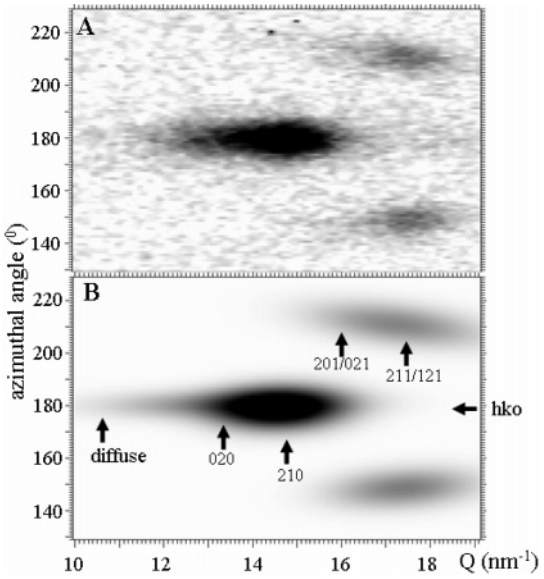

Figure 4. (A) Cake-regrouped degummed *B. mori* pattern covering the range of the strongest equatorial and first-layer line reflections; (B) simulated cake-regrouped pattern fitted by four 2D Gaussian profiles for 020, 210, and 201/021 + 211/121 reflections. An equatorial Gaussian profile extending toward the 010 position simulates residual diffuse scattering (same intensity scale for both patterns).

The pattern from a *B. mori* cocoon bave contains in addition scattering from sericin. The sericin volume fraction dominates the pattern obtained with a $1 \times 1\ \mu m^2$ fwhm beam at the edge of a bave (Figure 5A). The azimuthally averaged pattern can be fitted by two broad Gaussian profiles ($d_1 = 0.391$ nm; $d_2 = 0.223$ nm). The interpretation as short-range-order sericin scattering is corroborated by the fact that no evidence for such peaks has been obtained with a similar experiment on a degummed *B. mori* brin (not shown). A weak Gaussian profile at the position of the fibroin 020/210 peaks could be due to a small crystalline β-sheet fraction in sericin, but a small fraction of fibroin chains cannot be excluded (Figure 5B). It is, however, interesting to note that highly crystalline β-sheet material can be obtained by drying concentrated sericin solutions.[55] In addition, the high β-sheet content of recombinant sericin-like protein has been attributed to a long-range-ordered material.[56] This suggests that sericin might become amenable to single-crystal structure analysis by optimizing the crystallization conditions.

The pattern from the center of the bave (Figure 5C) will be dominated by fibroin scattering as the volume fraction of sericin in the microbeam gauge volume is only a few percent. The crystalline fibroin fraction will at any rate not be affected by the sericin scattering, which will contribute principally to the short-range-order peak. The 1D profile was fitted by four Gaussian profiles for the Bragg peaks, two broad peaks, and a zero-order polynomial background (Figure 5D). The broad peak at $Q \approx 15\ nm^{-1}$ corresponds to the sum of fibroin and (weak) sericin short-range-order scattering. The second sericin peak in Figure 5B overlaps with other diffuse and crystalline fibroin scattering contributions including the 040 Bragg peak.

Evolution of Peak Positions. The evolution of the peak positions of the strongest equatorial reflections during the in situ heating experiment is shown in Figures 6A and 6B. The data obtained for the *Greige* silk (Figure 6A) suggest that the lattice expansion follows two phases: a linear expansion phase up to 200−250 K and an enhanced linear expansion phase at higher temperatures. In this second phase, the thermal expansions derived from linear least-squares fits are 1×10^{-3} nm/K (210 reflection) and 1.8×10^{-3} nm/K (020 reflection). This implies a lower thermal expansion along the [210] direction, which is closer to the pleated-sheet [100] direction than to the chain-stacking [010] direction. In view of the overlap of 200 and 210 reflections, we verified that the thermal expansion derived from the 030 reflection was comparable to the 020 reflection. The position of the *B. mori* 002 reflection is practically constant across the temperature range (data not shown), which suggests that the peptide chain expansion coefficient along the *c*-axis expansion is significantly below the [210] and [010] expansion coefficients. Although less smooth due to poorer statistics, the results for fresh silk expansion seem to follow the same scheme (Figure 6B).

The origin of the onset of the enhanced thermal expansion into the [010] direction is not clear at present but could be due to an increasing side-chain mobility (e.g., onset of CH_3 rotation), modifying the interchain distance. An onset of molecular mobility at about 200 K has also been observed for dragline spider silk by inelastic neutron scattering[24] and dynamic mechanical analysis (DMA).[57] The neutron scattering data are, however, mainly due to water mobility in the amorphous chain fraction, while the current diffraction data reflect the crystalline fraction.

Evolution of Crystalline Fraction. The sum of intensities of the Bragg peaks ($\sum I_{Bragg}$), corresponding to the crystalline fraction, was separated from the short-range-order scattering by fitting Gaussian and polynomial profiles to the sequence of patterns (Supporting Information). $\sum I_{Bragg}$ remains practically constant during the in situ heating experiment up to 500 K. The data points shown in Figure 7 were scaled to the average of the values up to 450 K (1.0), which will be called a crystallinity index. This shows the high thermal stability of the crystalline fraction. There is notably no evidence for an increase in 210 intensity in this range, which excludes a contribution from the amorphous, random-coil fibroin to crystalline β-sheet transition at about 463 K.[58,59] This supports the assumption of a low random-coil volume fraction in *B. mori* silk fibers.[60] At ~550 K, the short-range-order scattering becomes dominant, and only the strongest equatorial Bragg peaks remain visible. At ~570 K, the equatorial Bragg peaks have disappeared, and the short-range-order peak has transformed into a more narrow powder ring, which has moved to a larger *Q*-value. The azimuthally integrated intensity profile of this pattern can be fitted by three Gaussian peaks and a zero-order polynomial background, suggesting the presence of residual diffuse halo and two new peaks, which will be discussed below (Figure 7). The loss in crystalline fraction coincides with a weight loss determined by thermogravimetry and CO_2 liberation due to chain scission determined by evolved gas detection.[9]

Evolution of the Amorphous Fraction. Figures 8A−C show the evolution of the Gaussian peak attributed to the short-range-order fraction with temperature (Figure 5D). The peak position remains practically constant up to about 430 K and decreases then up to 550 K (Figure 9A). At ~570 K, the sample has turned black, and the two new peaks shown in Figure 7 appear with a lattice spacing of $d = 0.34$ nm (strong) and $d = 0.21$ nm (weak), overlapping a remaining short-range-order peak ($d = 0.44$ nm). This supports carbonization as discussed for wood where the appearance of similar peaks has been attributed to the formation of turbostratic carbon.[61]

The evolution of the peak width shows an increase in the transition range 430 K < *T* < 550 K and then a significant

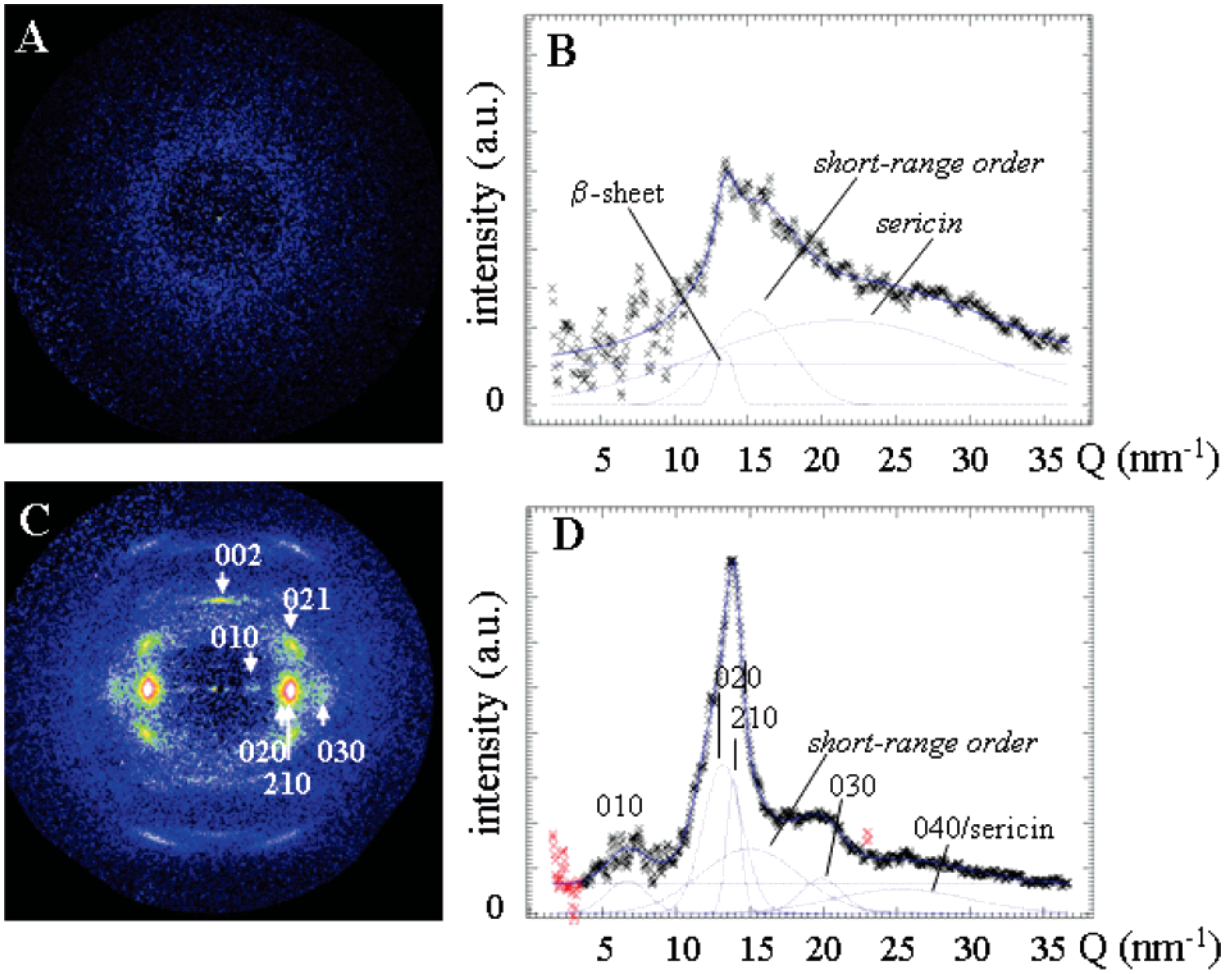

Figure 5. (A) *B. mori* pattern from the very edge of a bave; (B) 360° azimuthal average of part A. The pattern is fitted by a narrow Gaussian for the residual Bragg scattering, two broad Gaussians for the sericin short-range-order halo, and a zero-order polynomial for the random background. (C) Pattern from the center of one of the two brins in the bave; (D) azimuthal average across the equatorial peaks. The pattern is fitted by narrow Gaussians for the Bragg peaks, broad Gaussians for the short-range-order scattering, and a zero-order polynomial for the random background. (The red data points were masked during refinement.)

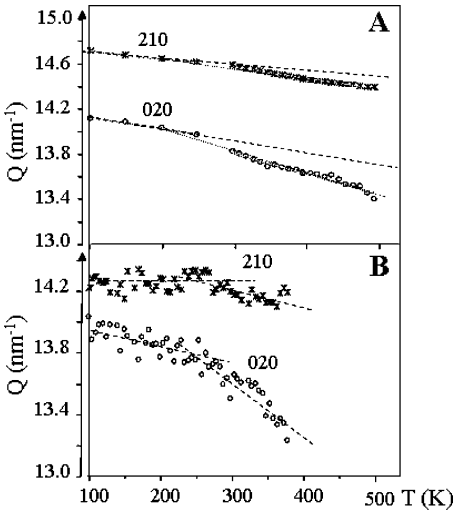

Figure 6. (A) Evolution of the position of the 210 (black stars) and 020 reflections (white circles) during the in situ heating of *Greige* silk; (B) same for fresh cocoon silk. Lines depicted are guidelines to the eye.

reduction as the new peak is formed at ~570 K (Figure 8B). The transition range shows also a slight increase in integrated peak intensity (Figure 8D). The origin of the transition range of 430 K < T < 550 K could be complex because the glass transition temperature for *B. mori* of 448 K[58] or 463 K[62] and an onset of weight loss[63] fall within this range. A degradation of intermolecular hydrogen bonding has been observed by IR spectroscopy in the temperature range of 423−453 K.[58] This suggests that the decrease of the peak position (Figure 8A) reflects a destruction of β-sheet bonding and hence an increasing [100] interchain distance, preceding carbonization.

Protein Stability. The result of protein analysis is shown in Figure 2B. FibH starts to degrade above ~350 K. This protein contains the (Gly-Ala)-rich sequences, which fold into crystalline β-sheet domains. As the crystal structure survives the molecular degradation (Figure 7), it is reasonable to assume that the degradation is limited to the random chains, connecting the crystalline domains. At 373 K, a degradation product of FibH can be observed as a light band under the native size FibH band, which suggests the existence of a site particularly sensitive to the thermal degradation (Figure 2B). SDS-PAGE (5% of acrylamide) without a stacking gel suggests a molecular weight of about 305 kDa for the degradation product. This degradation product could be due to one or several cleavages. FibL starts to degrade above about 400 K. This peptidic chain does not contain the (Ala-Gly)-rich regions folding into β-sheet domains. It is assumed to be part of the amorphous matrix embedding and linking them together, and it is more thermally stable than

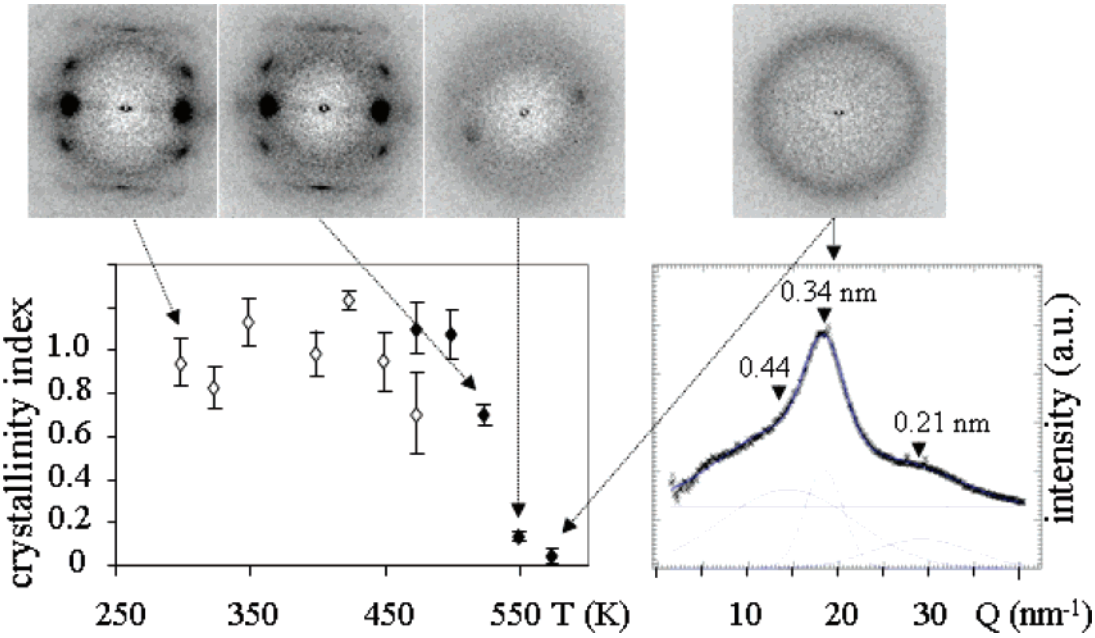

Figure 7. Evolution of the crystallinity index (see text) of the *B. mori* bave with temperature. The data were obtained from silk preheated in a nitrogen atmosphere (white diamonds) or in air (black diamonds). The values plotted are averages of the values calculated from seven to eight patterns for each fiber. The error bars are the standard deviations of these values. The selected diffraction patterns show the overall degradation. An azimuthally integrated intensity profile shown to the right has been determined for the pattern obtained at the highest temperature and fitted with three Gaussian profiles and a zero-order polynomial background. The *d*-values (nm) of the fitted peaks are indicated.

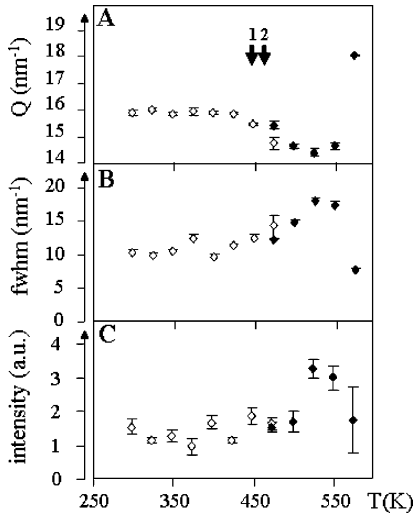

Figure 8. Evolution of profile parameters of a short-range-order halo, as shown in Figure 5D. The peak was fitted by a Gaussian profile with a polynomial background: (A) evolution of the peak position; (B) evolution of peak width (fwhm); (C) evolution of the integrated intensity. The open rhomboids correspond to samples, which were heated in nitrogen and then measured at room temperature; the filled rhomboids correspond to samples heated in air and then cooled to room temperature (see text) The vertical arrows in part A correspond to reported glass transitions: 1, ref 58; 2, ref 62.

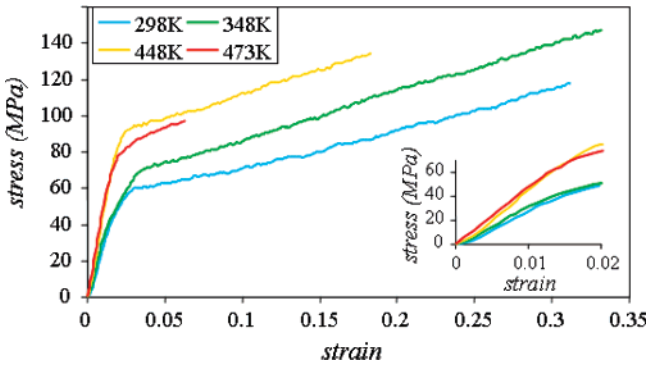

Figure 9. Stress−strain curves of a *B. mori* silk bave after heating in a nitrogen atmosphere (see Materials and Methods section).

FibH. It is linked to FibH by a disulfide bond and probably contains numerous hydrogen bonds that maintain the cohesion of the fiber.

Evolution of Mechanical Properties. *B. mori* and dragline silks can be considered as protein elastomers.[19] This is shown by the temperature-dependent stress−strain curves of *B. mori* baves heated in a nitrogen atmosphere, which resemble the transition from an elastomeric to a hard, ductile polymer[64] (Figure 9). The linear onset (Figure 9, inset) is attributed in analogy to dragline silk[24,30] to the deformation of a network of flexible, hydrogen-bonded chains, reinforced by crystalline domains. The decrease of the strain-to-failure for thermal treatments above about 350 K is reflected on the molecular scale by a degradation of the fibroin proteins (Figure 2B). A more detailed analysis of the mechanical parameters over a larger temperature range is shown in Figures 10A−C. The tensile strength and initial modulus values are scaled to the total bave cross-section (left ordinates). As the sericin contribution to the tensile deformation can practically be neglected,[65] we are reporting in Figures 10B and 10C also mechanical properties corrected for the sericin cross-section (right ordinates). *B. mori* silk shows a large variability of mechanical properties at the intraspecific and intraindividual levels.[5,66] Degumming[67] or variations in crystallinity along the fibers[32] also have been found to have an influence on the mechanical parameters. The sericin-corrected values reported in Figures 10B and 10C (right ordinates) correspond well to the range of values reported.[5,66]

We note that both strain-to-failure and tensile strength decrease above ~400 K while the modulus continues to rise up to nearly 500 K, which is at the onset of crystallinity decay (Figure 7). The 400 K limit of stress and strain increase corresponds about to the onset of FibL degradation (Figure 2B). The origin of these changes has to be located in the amorphous chain fraction as the crystalline domain fraction is not affected

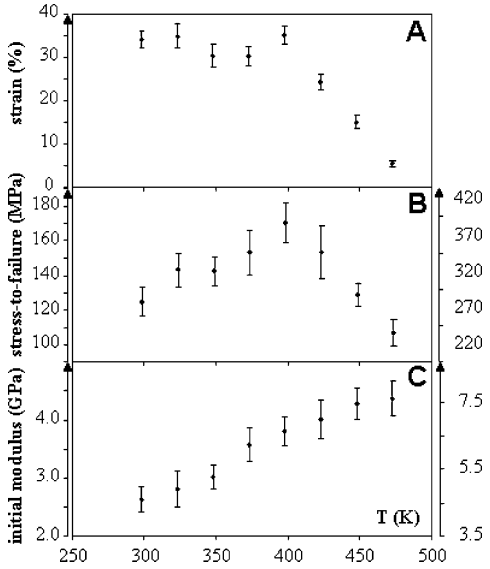

Figure 10. Evolution of mechanical properties of cocoon silk bave after heat treatment: (A) strain-to-failure; (B) tensile strength; (C) initial modulus. The left ordinate values in parts B and C have been scaled to the total bave cross-section; the right ordinate values in parts B and C have been scaled to the fibroin fraction (see text). The values plotted are averages of measurements from 9 to 15 baves for each temperature. The error bars correspond to the standard deviations of the individual samples divided by the square root of the number of samples.

(Figure 7). On the basis of protein analysis (Figure 2) it is suggested that cross-linking is starting at about 400 K due to chain scission resulting in the formation of $-NH_2$ and $-OH$ end groups. The reaction of these groups is assumed to produce cross-linking of neighboring chains. An increasing cross-link density with temperature can explain in analogy to elastomeric polymers[64] the increasing modulus while an increasing density of defects will reduce the strain-to-failure and stress-to-failure at the onset of cross-linking. The higher strain-to-failure and lower tensile modulus observed in this study with respect to previous studies can be attributed to the contribution of end effects over such short gauge lengths.

Conclusions

The structural data obtained on *B. mori* brins and baves support the model of a network of flexible polymer chains with hydrogen-bonding interactions, reinforced with crystalline β-sheet domains as for dragline silk.[24] A similar model has been proposed for *B. mori* silk based on electron diffraction/imaging[25] and used to model the mechanical properties of dragline silk.[30] The axial aggregation of β-sheet domains via short-range-order interface domains into nanofibrils[24] could not be verified but remains possible in view of SAXS[21,54] and TEM results.[25] A lateral aggregation of β-sheet units through van der Waals bonding is proposed to occur under conditions of drying and vacuum exposure. *B. mori* silk differs therefore from dragline silk by the lack or low amount of a short-range-order fraction in the (hypothetical) nanofibrils.

Short-range-order sericin scattering has been observed for the first time by SR microdiffraction at the edge of a bave. A small sericin crystallinity and results from other crystallization experiments suggest that single-crystal growth and structure analysis of sericin might become possible.

The present results show that the crystalline domains of *B. mori* silk start degrading only above about 500 K, which is comparable to dragline silk.[27] The thermal degradation of FibH and FibL molecules starting already in the range of 350−400 K affects thus only the short-range-order chain fraction. The mechanical properties such as ultimate tensile stress and strain-to-failure start to degrade at the onset of the FibH and FibL molecular degradation, suggesting a causal link. This and an increase in Young's modulus up to about 475 K indicate that degradation in the amorphous fraction is accompanied by an increasing cross-linking. The close analogy to elastomeric polymers suggests that models involving molecular springs[68] are not required for describing the mechanical properties.

Acknowledgment. The authors thank G. Chavancy (Unité Nationale Séricicole, INRA, Lyon, France) for a gift of *B. mori* cocoons, G. Freddi (Stazione Sperimentale per la Seta, Milano, Italy) for a gift of degummed *B. mori* silk, and N. Zafeiropoulos (Dresden, Germany) for helpful discussions. We gratefully acknowledge the help provided by L. Terradot-Piot (Partnership for Structural Biology Unit, Grenoble, France) with protein electrophoresis experiments, C. Koenig (ESRF) for help with laser microdissection, and I. Snigireva (ESRF) for the SEM images.

Supporting Information Available. Specialist batch processing software for analyzing a sequence of diffraction patterns. This material is available free of charge via the Internet at http://pubs.acs.org.

References and Notes

(1) Marsh, R. E.; Corey, R. B.; Pauling, L. *Biochim. Biophys. Acta* **1955**, *16*, 1−34.
(2) Lucas, F.; Shaw, J. T. B.; Smith, S. G. *Advances in Protein Chemistry 13*, Anfinsen, C. B., Anson, M. L., Bailey, K., Edsall, J. T., Eds., Academic Press; New York, 1956.
(3) *The Silk Fibroins*; Lucas, F. F., Shaw, J. T. B., Smith, S. G., Eds.; Advances in Protein Chemistry 13; Academic Press: New York, 1958.
(4) Fraser, R. D. B.; MacRae, T. P. *Conformations of Fibrous Proteins*; Academic Press: New York, 1973.
(5) *Silks: Chemistry, Properties, and Genetics*; Kaplan, D. L., Lombardi, S. J., Muller, W. S., Fossey, S. A., Eds.; Stockton Press: New York, 1991.
(6) Takahashi, Y.; Gehoh, M.; Yuzuriha, K. *Int. J. Mol. Biol.* **1999**, *24*, 127−138.
(7) Shao, Z.; Vollrath, F. *Nature* **2002**, *418*, 741−741.
(8) Hu, X.; Kaplan, D.; Cebe, P. *Macromolecules* **2006**, *39*, 6161−6170.
(9) Tsukada, M. *J. Appl. Polym. Sci.* **1978**, *22*, 543−554.
(10) Tanaka, K.; Inoue, S.; Mizuno, S. *Insect Biochem. Mol. Biol.* **1999**, *29*, 269−276.
(11) Inoue, S.; Tanaka, K.; Arisaka, F.; Kimura, S.; Ohmoto, K.; Mizuno, S. *J. Biol. Chem.* **2000**, *275*, 40517−40528.
(12) Inoue, S.; Tanaka, K.; Tanaka, H.; Ohmoto, K.; Kanda, T.; Imamura, M.; Kojima, G. X.; Yamashita, T.; Nakajima, T.; Taira, H.; Tamura, T.; Mizuno, S. *Eur. J. Biochem.* **2004**, *271*, 356−366.
(13) Tanaka K., K. N.; Ishikura, K.; Waga, S.; Kikuchi, A.; Ohtomo, K.; Takagi, T.; Mizuno, S. *Biochim. Biophys. Acta* **1999**, *1432*, 92−103.
(14) Gamo, T.; Inokuchi, T.; Laufer, H. *Insect Biochem.* **1977**, *7*, 285−295.
(15) *Silk Polymers: Materials Science and Biotechnology*; Kaplan, D. L., Adams, W. W., Viney, C., Farmer, B. L., Eds.; ACS Symposium Series 544; American Chemical Society: Washington, DC, 1994.
(16) Ha, S. W.; Park, Y. H.; Hudson, S. M. *Biomacromolecules* **2003**, *4*, 488−496.
(17) Geourjon, C.; Deléage, G. *Comput. Appl. Biosci.* **1995**, *11*, 681−684.
(18) Raghava, G. P. S. APSSP2: A combination method for protein secondary structure prediction based on neural network and example based learning, accessed July 10, 2007. http://www.forcasp.org/paper1817.html.
(19) Vollrath, F.; Porter, D. *Soft Matter* **2006**, *2*, 377−385.
(20) Shear, W. A.; Palmer, J. M.; Coddington, J. A.; Bonamo, P. M. *Science* **1989**, *246*, 479−481.

(21) Miller, L. D.; Putthanarat, S.; Eby, R. K.; Adams, W. W. *Int. J. Mol. Biol.* **1999**, *24*, 159−165.
(22) Putthanarat, S.; Stribeck, N.; Fossey, S. A.; Eby, R. K.; Adams, W. W. *Polymer* **2000**, *41*, 7735−7747.
(23) Yang, Z.; Grubb, D. T.; Jelinski, L. W. *Macromolecules* **1997**, *30*, 8254−8261.
(24) Sapede, D.; Seydel, T.; Forsyth, T.; Koza, M. M.; Schweins, R.; Vollrath, F.; Riekel, C. *Macromolecules* **2005**, *38*, 8447−8453.
(25) Shen, Y.; Johnson, M. A.; Martin, D. C. *Macromolecules* **1998**, *31*, 8857−8864.
(26) Oroudjev, E.; Soares, J.; Arcidiacono, S.; Thompson, J. B.; Fossey, S. A.; Hansma, H. G. *Proc. Natl. Acad. Sci. U.S.A.* **2002**, *99*, 6460−6465.
(27) Glišovic, A.; Salditt, T. *Appl. Phys. A: Mater. Sci. Process.* **2007**, *87*, 63−69.
(28) Grubb, D. T.; Jelinski, L. W. *Macromolecules* **1997**, *30*, 2860−2867.
(29) Riekel, C.; Bränden, C.; Craig, C.; Ferrero, C.; Heidelbach, F.; Müller, M. *Int. J. Mol. Biol.* **1999**, *24*, 187−195.
(30) Termonia, Y. *Macromolecules* **1994**, *27*, 7378−7381.
(31) Bram, A.; Branden, C.; Craig, C.; Snigireva, I.; Riekel, C. *J. Appl. Crystallogr.* **1997**, *30*, 390−392.
(32) Sinsawat, A.; Puttharanat, S.; Magoshi, Y.; Pachter, R.; Eby, R. K. *Polymer* **2002**, *43*, 1323−1330.
(33) Freddi, F.; Tsukada, M. In *Polymeric Materials Encyclopedia*; Salamone, J. C., Ed.; CRC Press: Boca Raton, FL, 1996; Vol. 10, pp 7734−7744.
(34) Oxford Cryosystems. Cryostream plus, accessed July 10, 2007. http://www.oxfordcryosystems.co.uk/cryostream/plusdownloads.htm.
(35) Hammersley, A. The FIT2D home page, accessed July 10, 2007. http://www.esrf.eu/computing/scientific/FIT2D/.
(36) Riekel, C. *Rep. Prog. Phys.* **2000**, *63*, 233−262.
(37) Perrakis, A.; Cipriani, F.; Castagna, J. C.; Claustre, L.; Burghammer, M.; Riekel, C.; Cusack, S. *Acta Crystallogr., Sect. D: Biol. Crystallogr.* **1999**, *55*, 1765−1770.
(38) Schroer, C. G.; Kuhlmann, M.; Lengeler, B.; Günzler, T. F.; Kurapova, O.; Benner, B.; Rau, C.; Simionovici, A. S.; Snigirev, A.; Snigireva, I. Beryllium parabolic refractive X-ray lenses. In *Design and Microfabrication of Novel X-ray Optics*; Mancini, D. C., Ed.; Proceedings of SPIE 4783; SPIE: Bellingham, WA, 2002; pp 10−18.
(39) Takahashi, Y. In *Silk Polymers: Materials Science and Biotechnology*; Kaplan, D., Adams, W. W., Farmer, B., Viney, C., Eds.; ACS Symposium Series 544; American Chemical Society: Washington, DC, 1994; pp 168−175.
(40) Müller, M.; Burghammer, M.; Flot, D.; Riekel, C.; Morawe, C.; Murphy, B.; Cedola, A. *J. Appl. Crystallogr.* **2000**, *33*, 1231−1240.
(41) Schoeck, J.; Davies, R. J.; Martel, A.; Riekel, C. *Biomacromolecules* **2007**, *8*, 602−610.
(42) Blanton, T. N.; Huang, T. C.; Toraya, H.; Hubbard, C. R.; Robie, S. B.; Louer, D.; Goebel, H. E.; Will, G.; Gilles, R.; Raftery, T. *Powder Diffr.* **1995**, *10*, 91−95.
(43) Davies, R. *J. Appl. Crystallogr.* **2006**, *39*, 267−272.
(44) Thiel, B. L.; Kunkel, D.; Viney, C. *Biopolymers* **1994**, *34*, 1089−1097.
(45) Ruland, W. *Acta Crystallogr.* **1961**, *14*, 1180−1185.
(46) *X-ray Synchrotron Radiation Microdiffraction on Fibrous Biopolymers Like Cellulose and in Particular Spider Silks*; Burghammer, M., Müller, M., Riekel, C., Eds.; Research Signpost: Trivandrum, India, 2003; Vol. 7.
(47) Somashekar, R.; Urs, R. G.; Madhava, M. S. *J. Appl. Polym. Sci.* **1992**, *44*, 2161−2165.
(48) Klug, H. P.; Alexander, L. E. *X-ray Diffraction Procedures for Polycrystalline and Amorphous Materials*, 2nd ed.; Wiley: New York, 1974.
(49) Roessle, M.; Panine, P.; Urban, V. S.; Riekel, C. *Biopolymers* **2004**, *74*, 316−327.
(50) Iizuka, E. *Biorheology* **1965**, *3*, 1−8.
(51) Kennedy, C. J.; Lerber, K. v.; Wess, T. J. *e-Preserv. Sci.* **2005**, *2*, 31−37.
(52) Nadiger, G. S.; Halliyal, V. G. *Colourage* **1984**, *31*, 23−32.
(53) Yanagi, Y.; Kondo, Y.; Hirabayashi, K. *Text. Res. J.* **2000**, *70*, 871−875.
(54) Londono, J. D.; Annadurai, V.; Gopalkrishne, R.; Somashekar, R. *J. Appl. Polym. Sci.* **2002**, *85*, 2382−2388.
(55) Knight, D.; Riekel, C. Unpublished work, 2007.
(56) Huang, J.; Valuzzi, R.; Bini, E.; Vernaglia, B.; Kaplan, D. L. *J. Biol. Chem.* **2003**, *278*, 46117−46123.
(57) Cunniff, P. M.; Fossey, S. A.; Auerbach, M. A.; Song, J. W. In *Silk Polymers: Materials Science and Biotechnology*; Kaplan, D., Adams, W. W., Farmer, B., Viney, C., Eds.; ACS Symposium Series 544; American Chemical Society: Washington, DC, 1994; pp 234−251.
(58) Nakamura, S.; Magoshi, J.; Magoshi, Y. In *Silk Polymers: Materials Science and Biotechnology*; Kaplan, D., Adams, W. W., Farmer, B., Viney, C., Eds.; ACS Symposium Series 544; American Chemical Society: Washington, DC, 1994; pp 211−221.
(59) Magoshi, J.; Magoshi, Y.; Nakamura, S.; Kasai, N.; Kakudo, M. *J. Polym. Science: Polym. Phys. Ed.* **1977**, *15*, 1675−1683.
(60) Yao, J.; Nakazawa, Y.; Asakura, T. *Biomacromolecules* **2004**, *5*, 680−688.
(61) Saito, Y.; Arima, T. *J. Wood Sci.* **2004**, *50*, 87−92.
(62) Tsukada, M.; Freddi, G.; Nagura, M.; Ishikawa, H.; Kasai, N. *J. Appl. Polym. Sci.* **1992**, *46*, 1945−1953.
(63) Shirakashi, K.; Takubo, T.; Takahashi, Y. Y. *Sen'i Kogyo Gakkaishi* **1942**, *8*, 119.
(64) Nielsen, L. E.; Landel, R. F. *Mechanical Properties of Polymers and Composites*, 2nd ed.; Marcel Dekker: New York, 1994.
(65) Perez-Rigueiro, J.; Viney, C.; Llorca, J.; Elices, M. *J. Appl. Polym. Sci.* **2000**, *175*, 1270−1277.
(66) Zhao, H. P.; Feng, X. Q.; Shi, H. J. *Mater. Sci. Eng., C* **2007**, *27*, 675−683.
(67) Perez-Rigueiro, J.; Elices, M.; Llorca, J.; Viney, C. *J. Appl. Polym. Sci.* **2002**, *84*, 1431−1437.
(68) Becker, N.; Oroudjev, E.; Mutz, S.; Cleveland, J. P.; Hansma, P. K.; Hayashi, C. Y.; Makarov, D. E.; Hansma, H. G. *Nat. Mater.* **2003**, *2*, 278−283.

BM700935W